Received: 17 May 2018 | Revised: 3 February 2019 | Accepted: 24 July 2019

DOI: 10.1002/jnm.2674

EMF18 SPECIAL ISSUE

WILEY

Modeling of history-dependent magnetization in the finite element method on the example of a postassembly rotor magnetizer

Gregor Bavendiek | **Fabian Müller** | **Simon Steentjes** | **Kay Hameyer**

Institute of Electrical Machines (IEM), RWTH Aachen University, Schinkelstrasse 4, Aachen, Germany

Correspondence
Gregor Bavendiek, Institute of Electrical Machines (IEM), RWTH Aachen University, Schinkelstrasse 4, 52062 Aachen, Germany,
Email: Gregor.Bavendiek@iem.rwth-aachen.de

Present Address
Gregor Bavendiek, Schinkelstrasse 4, 52062 Aachen, Germany.

Funding information
Deutsche Forschungsgemeinschaft, Grant/Award Number: project: 373150943

Abstract

Demagnetization characteristics of permanent magnets play a central role for the design and optimization process of permanent magnet electrical machines and magnetic actuators. Currently, practical issues, such as loss of performance of electromagnetic energy conversion devices, due to demagnetization effects in permanent magnets or due to reduced servo-dynamics in magnetic actuators, cannot be addressed by using conventional material models or are investigated by using rough approximations valid in restricted operation regions, if at all. This paper strives to integrate demagnetizing characteristics dependent on previous magnetizing field strength in the finite element method. The discussed examples are a magnetizer of a single permanent magnet and a spoke-type permanent magnet rotor.

KEYWORDS

demagnetization, magnetic hysteresis, magnetization processes, permanent magnets

1 | INTRODUCTION

After manufacturing, permanent magnets are magnetized to possess a remanent magnetic polarization for serving as a source of magnetic field. To reach full magnetization, very high magnetic field strengths, H in A/m, are necessary, as a rule of thumb at least three to five times of coercivity, H_c. Impulse magnetizers are utilized to impose such high magnetic field strengths into permanent magnets. In the case of permanent magnet machine rotors, the permanent magnets can either be magnetized within the rotor or before being mounted into the rotor, but then they are mechanically hard to handle, and a self-degaussing occurs, which is dependent on the form factor.[1] A current research question is the postassembly magnetization of permanent magnets in a machine rotor.[2,3] In order to achieve the best utilization of the permanent magnet material, a basic understanding of the magnetization process and its simulation is required.

2 | MODELING OF PERMANENT MAGNET DEMAGNETIZATION DEPENDING ON MAGNETIZATION FIELD

2.1 | Classical approaches

The relative permeability of fully magnetized rare-earth permanent magnets is close to one in the first and second quadrant of $B(H)$ characteristic, which is why there occurs almost no irreversibility.[4] The simplest models correspond to an analytical linear or nonlinear equation. A single hyperbolic tangent function already forms a good approximation of the scalar magnetic polarization in preferred direction over the magnetic field strength. In Zhou et al,[5] the scalar demagnetization curve in preferred direction, J in T, of fully magnetized permanent magnets is illustrated by two hyperbolic tangent functions as follows:

$$J(H)=\left(b_0 tanh\left(\frac{H+H_c}{h_0}\right)+b_1 tanh\left(\frac{H+H_c}{h_1}\right)\right). \tag{1}$$

The coefficients $b_{0,1}$ describe the magnetic remanence and $h_{0,1}$ the occurring knee field strength. Due to Ampere's law, a coercive field strength can be recalculated into an equivalent source current, which is used in standard finite element method (FEM) approaches to model nonlinear permanent magnet behavior in third and fourth quadrants as follows:

$$\vec{\nabla} \times \vec{H}_c = \vec{J}_{PMsource} \tag{2}$$

Taking this additional source into account, on the excitation side of Equation (4), a remanent magnetic polarization is represented. The equivalent current source moves the magnetization curve inside the permanent magnet to the

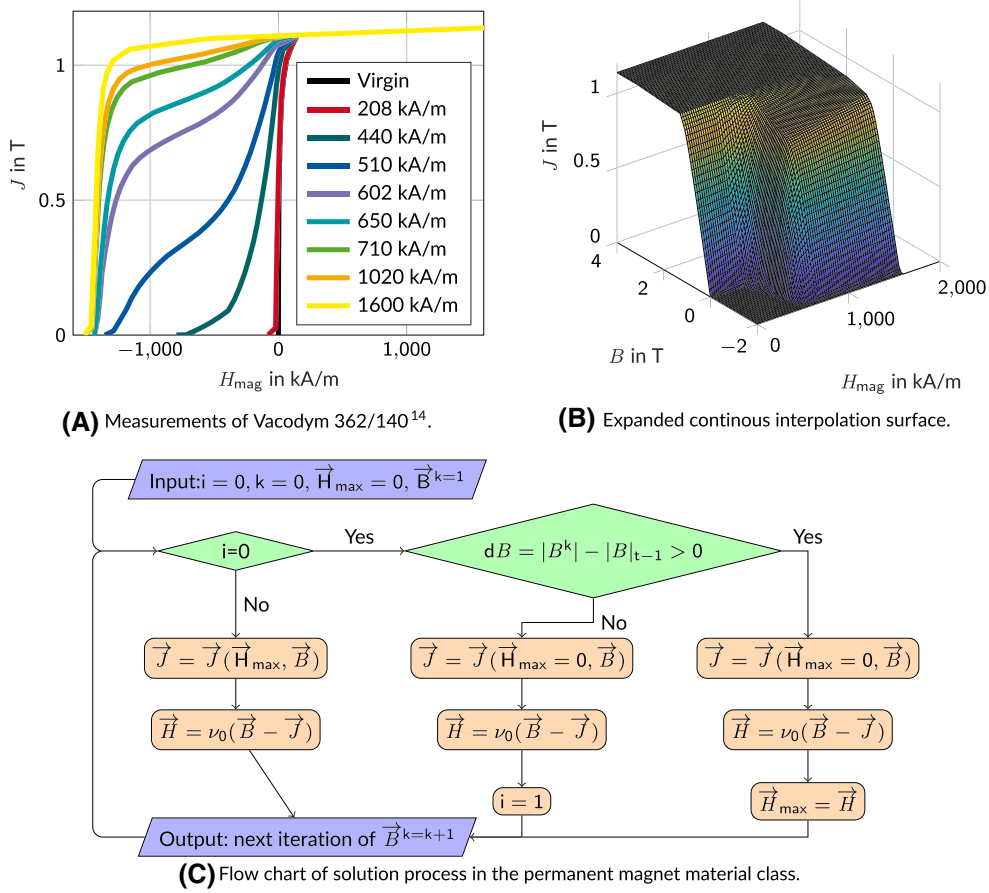

(A) Measurements of Vacodym 362/140[14]. **(B)** Expanded continous interpolation surface.

(C) Flow chart of solution process in the permanent magnet material class.

FIGURE 1 Dependancy of magnetic polarization on magnetizing field Dependency of magnetic polarization on magnetizing field, a) Measurements, b) Data processing, c) Algorithm of simulation

origin, which produces a symmetrical scalar magnetization curve in the first and third quadrants, equivalent to the modeling of soft magnetic materials.[6] This single characteristic is not variable during the simulation, and therefore, only represents a reversible demagnetization curve without dependency from previous magnetization.

In addition, various hysteresis models have been transferred to permanent magnets or developed especially for them, such as the ferromagnetic positive-feedback theory.[7] Simple mathematical models are pice-wise-linear[8] and transplantation type, such as Tellinen[9] or Zirka.[10] Popular models are the Jiles-Atherton[11] or Preisach[12] and Play.[13] Unfortunately, most hysteresis models only produce symmetric curves, which are not capable of representing inner virgin magnetization loops, as the ones shown in Figure 1A. Therefore, the focus of this paper is on the nonlinear magnetization, field-dependent demagnetization characteristic, which later still can be integrated into a mathematical hysteresis model, such as the Tellinen, which is related to Equation 1.

2.2 | Continuous history-dependent (de-)magnetization surface

Permanent magnets are operated as a field source in the second quadrant of $B(H)$ characteristic.[4] For that, the virgin magnetization curve must be run through to saturation first. Depending on the maximum field strength experienced of the permanent magnet, different demagnetization characteristics occur, as illustrated in Figure 1A. Based on a common virgin curve in the first quadrant, depending on the maximum field strength seen by the hard magnetic material during magnetization process, the demagnetization curves split with nonlinear courses in the second quadrant. While for high magnetizing field strength, the demagnetization curves are almost linear up to the knee point; the demagnetization curves at low magnetizing field strength have saddled and turning points, Figure 1A. According to the previous elaborations, it can be concluded that the previously presented analytical model with only one demagnetization curve is not suitable for the description of a magnetization process of permanent magnet material.

In this paper, a history-dependent permanent magnet material model is proposed, which stores the magnetization field strength occurring in each element during the transient magnetization process. First, while increasing impulse magnetization, the virgin magnetization curve is utilized. Second, as soon as the magnetization process reaches its peak, a demagnetizing curve is selected in each element, which is related to the maximum magnetization field strength. Subsequently, the material equation is solved as follows:

$$\overrightarrow{H} = \nu_0(\overrightarrow{B} - \overrightarrow{J}_{PMsurface}(\overrightarrow{B}, \overrightarrow{H}_{mag})). \tag{3}$$

For simplicity, it is assumed that a remanent magnetic polarization only appears in the preferred magnetization direction. All other directions have a linear characteristic with relative permeability close to one. The necessary material data for calculation, as shown in Figure 1B, is derived by interpolation of the measured material data from the Vacuumschmelze catalog, as shown in Figure 1A. The interpolation surface is directly derived from measurements, which may contain measurement deviations, causing nonphysical behavior. Thus, a regularization algorithm has to be applied to avoid numerical instability. A regularization method can be the application of an analytical equation, such as Equation (1) to the scalar magnetization in preferred direction $J(H)$ and a sigmoid function to the corresponding $J(H_{mag})$. In this paper, a two-dimensional smoothing spline is directly applied to the measurements, which result in the surface shown in Figure 1B. The flow chart for the determination of the magnetic polarization is depicted in Figure 1C.

3 | FINITE ELEMENT METHOD

$$\overrightarrow{\nabla} \times (\nu \overrightarrow{\nabla} \times \overrightarrow{A}) + \sigma \frac{\partial \overrightarrow{A}}{\partial t} = \overrightarrow{J}_{source} \text{ with } \overrightarrow{B} = \overrightarrow{\nabla} \times \overrightarrow{A} \text{ and } \overrightarrow{H} = \nu \overrightarrow{B}. \tag{4}$$

In the considered case of a rotor magnetizer, the general Maxwell equations can be simplified and merged into a quasi-static magnetic vector potential formulation to calculate the transient electromagnetic fields, as in Equation 4. The equation is derived from the combination of Ampere's law with the neglection of displacement current density[15] and the magnetic material law. The reluctivity ν can be a scalar, a scalar function, or a tensor of second rank. The time derivative of the magnetic vector potential is calculated by an implicit Euler scheme. The previously defined equation must be fulfilled in the entire solution area in compliance with all constraints, such as sub-areas with different

materials, boundary conditions, and impressed excitations. Complex considered geometries have to be solved either in two or three dimensions. The magnetic vector potential A is a function of space and time and is discretized over geometry by means of finite elements. The magnetic vector potential $\vec{A}$ represents an approximation to the true Solution $\vec{A}^*$. The absolute error is called residual and is calculated by Equation (5).

$$\vec{\nabla} \times \vec{H} - \vec{J}_{source+eddy} = \vec{R}\ ,\ \vec{R} \xrightarrow[\vec{A} \to \vec{A}^*]{} 0. \tag{5}$$

The material behavior depicted in the last chapter needs to be considered for a sufficient solution, which is why a suitable iteration method for nonlinearity needs to be applied.[16] Because of its fast convergence speed, the Newton method is applied.[17] The Newton method calculates the correction $\Delta\vec{A}$ by linearizing the material behavior in the current working point, represented by the Jacobian matrix P. The error in Equation (5) is minimized by the following equation:

$$P^k \Delta\vec{A}^k = \vec{R}(\vec{A}^k) \quad = \vec{J} - \vec{\nabla} \times \vec{H}(\vec{B}^k). \tag{6}$$

The derivative of the resudial in terms of the magnetic vector potential $\left(\frac{\partial R}{\partial A}\right)$ is called Jacobi matrix.[18] The evaluation of the Jacobi matrix, which is referred to as P, requires the correct evaluation of the derivatives[19]

$$(P)_{ij} = \left(\frac{\partial R_i}{\partial A_j}\right) = \int_\Omega \vec{\nabla} \times \alpha_i \cdot \left[\frac{\partial H_i}{\partial B_j}\right] \cdot \vec{\nabla} \times \alpha_j \, d\Omega \quad with \frac{\partial H_i}{\partial B_j} = \frac{H_{i,k} - H_{i,k-1}}{B_{j,k} - B_{j,k-1}} = \begin{pmatrix} \frac{\partial H_x}{\partial B_x} & \frac{\partial H_x}{\partial B_y} & \frac{\partial H_x}{\partial B_z} \\ \frac{\partial H_y}{\partial B_x} & \frac{\partial H_y}{\partial B_y} & \frac{\partial H_y}{\partial B_z} \\ \frac{\partial H_z}{\partial B_x} & \frac{\partial H_z}{\partial B_y} & \frac{\partial H_z}{\partial B_z} \end{pmatrix}$$

$$= \nu_{d,ij}\ ,\ i,\ j \in [x, y, z]. \tag{7}$$

The entries within P^k are defined according to the different material regions. With a full consideration of the material properties, especially in the case of anisotropic materials, all entries must be evaluated. In this work, the assumption is made that the nonpreferred direction of permanent magnet regions behaves like air and is therefore not coupled to the preferred direction, which leads to a diagonal Jacobian matrix. Due to these restrictions, the Newton method does not evaluate the exact Jacobi matrix, but an approximation, which is why this modified method is a quasi Newton.

4 | APPLICATION OF HISTORY-DEPENDENT PERMANENT MAGNET MODEL

4.1 | Impulse magnetizer for single magnet

The geometry of an impulse magnetizer, taken from Przybylski et al,[20] for a single magnet is shown in Figure 2A in 2-D and Figure 2 B in 3-D. Due to symmetry conditions, a quarter model is sufficient for 2-D simulation and an eighth for 3-D. The modeled surrounding air is large, in order not to affect the stray fields.

The magnetizing circuit, as shown in Figure 3A, consists of an interconnection of a capacity $C1$ and a magnetizing coil $L1$. The capacity is initially charged and then shorted over the coil via a thyristor $Thy1$. A corresponding pulse current is shown in Figure 3B. The current amplitude is 1200 A multiplied by 440 winding turns. The simulation time is divided into 500 equidistant time steps. The capacity must be big enough to provide the necessary magnetization energy and the additional (Ohmic) losses. The requirement for the magnetizing coil is to provide the required field distribution in the most homogeneous way possible, despite inhomogeneities due to geometry and eddy currents.

The 2-D model in Cartesian coordinates is an approximation of the axial symmetric geometry and causes deviations in local field and eddy currents. Nevertheless, the 2-D and 3-D simulations are in good agreement, see Figures 4 and 5. The major effect is the magnetizing field-dependent demagnetization in addition to a minor effect due to local eddy currents.

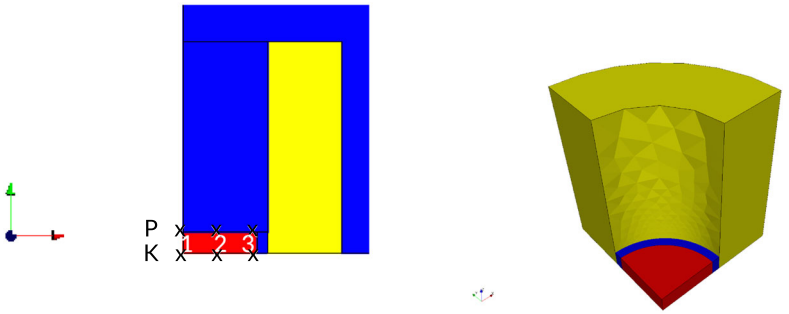

(A) Geometry 2D (red=Permanent Magnet, yellow=Magnetizaition Winding, blue=Surrounding Air).

(B) Geometry 3D (red=Permanent Magnet, yellow=Magnetizaition Winding, blue= Airgap (surroundings hidden)).

FIGURE 2 Geometry of impulse magnetizer for single magnet, see Przybylski et al[20]

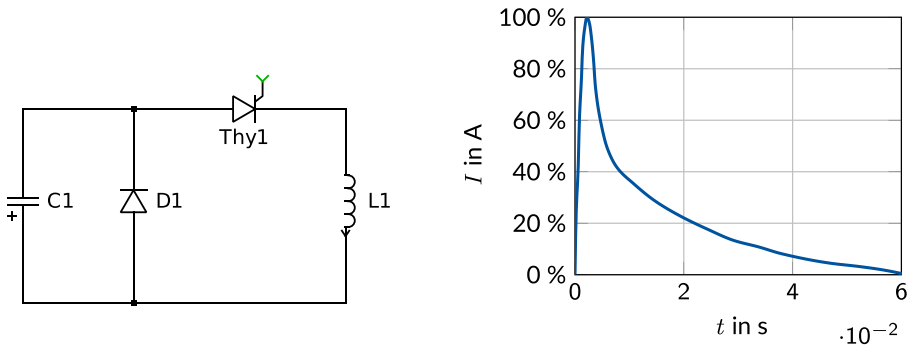

(A) Circuit. **(B)** Impulse current.

FIGURE 3 Electric circuit of impulse magnetizer for single magnet, see Przybylski et al[20]

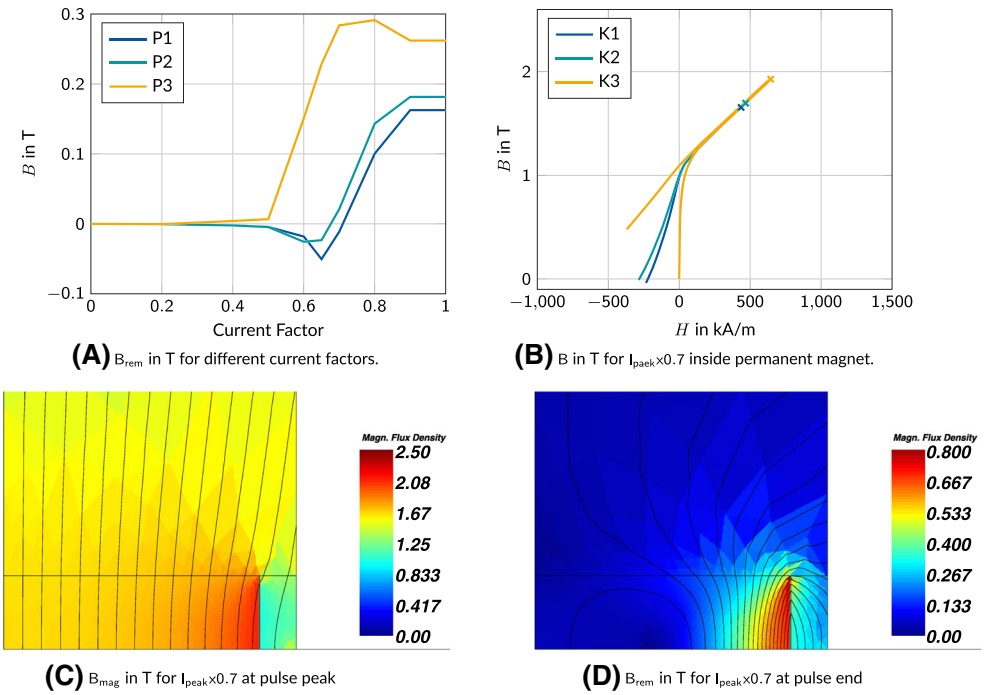

(A) B_{rem} in T for different current factors. **(B)** B in T for I_{paek}×0.7 inside permanent magnet.

(C) B_{mag} in T for I_{peak}×0.7 at pulse peak **(D)** B_{rem} in T for I_{peak}×0.7 at pulse end

FIGURE 4 Local magnet flux distribution inside the permanent magnet during and after impulse magnetization

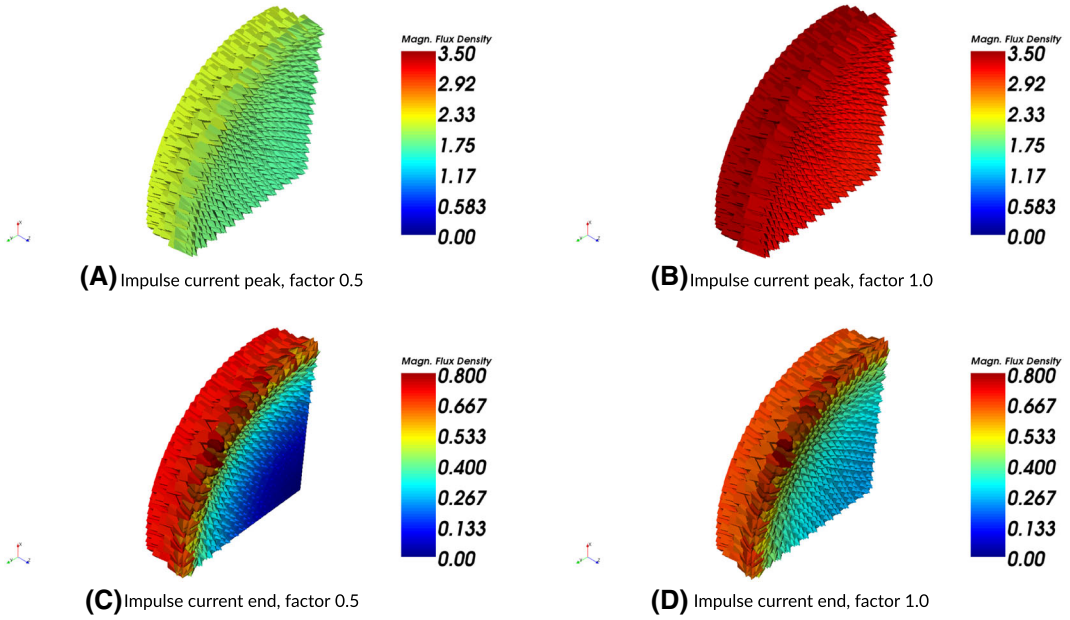

FIGURE 5 Local flux density distribution in 3-D sample

The influence of the magnetizing field strength-dependent demagnetization is demonstrated by simulations at scaled magnetizing current I_{peak} from 20% up to 100%. The values for the magnetic flux density and magnetic field strength are extracted at the points K (1, center; 3, edge; and 2, in-between) inside the permanent magnet in preferred magnetization direction; the points P are the corresponding ones at the surface of the permanent magnet. As an example, the magnetic flux for the impulse current factor of 0.7 is shown at three points inside the permanent magnet over the full simulation time in Figure 4B and for the peak, as well as the end of impulse current over the geometry in Figure 4C and 4D, respectively. The measurements in Przybylski et al[20] correspond to the simulation in this paper, with the difference of another NdFeB material (VACODYM 362/140). A validation of the method concerning the same material is given in Bavendiek et al.[21]

At the first glance of Figure 4A, it is contradictory that although the outer field acts only in one direction, the remanent magnetization of the magnet changes its polarity from center ($P1$) to edge ($P3$). The reason for that is the inhomogeneous magnetizing field strength during transient impulse magnetization, increased by local eddy currents, causing different demagnetization resistances. That results in self-degaussing of the strong magnetized edges through the weak magnetized center of the permanent magnet. This inhomogeneity of magnetic flux density is particularly visible in the flux distributions of the 3-D simulations in Figure 5. The permanent magnet magnetizes with its virgin curve at increasing pulse current. The magnetic flux density reaches its maximum almost at the peak value of the pulse current, Figure 5A and 5B. The corresponding maximum magnetization field strength determines the demagnetization curve at descending pulse current. At the end of the pulse current, only the remanent magnetization remains, Figure 5C and 5D. However, the inhomogeneity then increases due to different demagnetization resistance. This effect leads to the fact that the local remanence considerably deviates from the measured mean magnetization measured by a flux meter or hysterograph. The goal is to ensure the maximum demagnetizing field strength in all regions of the magnet with minimal energy.

4.2 | Postassembly magnetizer for spoke-type rotor

This section deals with the magnetizing process of a spoke-type permanent magnet rotor. To reduce the self-degaussing and to simplify the installation of permanent magnets in the rotors, the magnetization is postassembly. This simplifies the installation of the magnets as they are inserted into pockets in the rotor or glued to the surface. In the literature,[22,23] a magnetic circuit model is applied for modeling the magnetization process. In comparison, in this paper, the approach described above is applied to a transient FEM simulation.

The sample topology of a spoke-type rotor of a permanent magnet synchronous machine is shown in Figure 6. Despite the geometry is not corresponding to any real machine in terms of its dimensions, all the fundamental effects

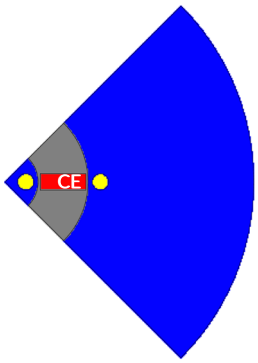

	Size in mm
Inner coil center	25
Inner rotor radius	40
Outer rotor radius	100
Outer coil center	115
Coil radius booth	10
Permanent magnet height	55
Permanent magnet width	20

FIGURE 6 Rotor magnetizer (yellow, magnetization winding; blue, surrounding air; red, magnet; gray, rotor lamination)

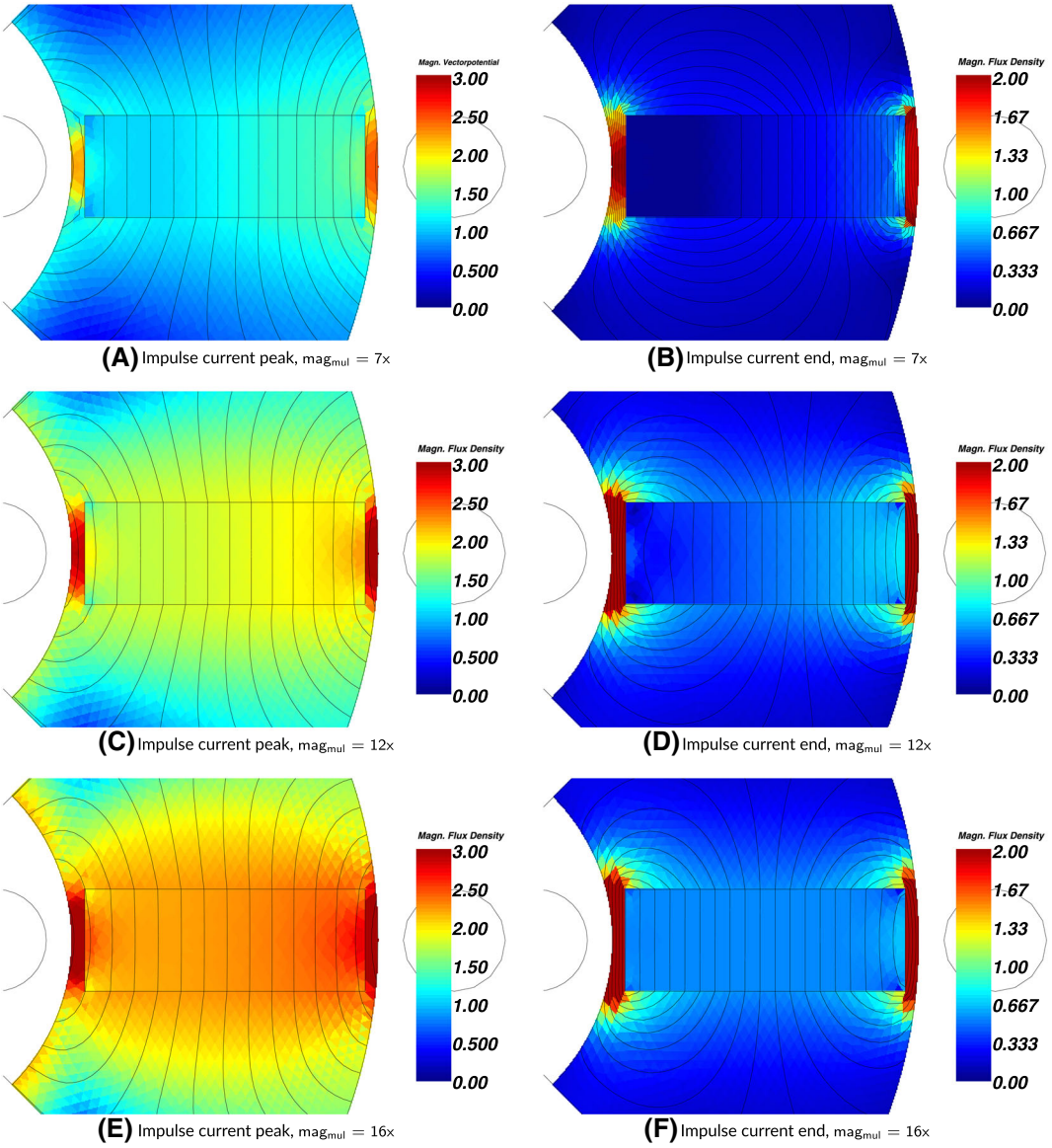

FIGURE 7 Local flux density distribution for different excitations

can be discussed here. Due to symmetry, the simulation is carried out by using only a quarter model with antiperiodic boundary conditions assigned to the limiting nodes that lie on the margin lines at ±45ř. This links the nodes so that the flow on those lines has a reverse sign. This corresponds to the opposing field of the next poles of the geometry at ±90ř. The inner rotor radius is 40 mm, and the outer one 100 mm. The two magnetization coils have a radius of 10 mm and

located at 25 mm and 115 mm. The permanent magnet with the dimensions of 55 Œ 20 mm is centered inside the rotor. This leads to a varying thickness of the surrounding electrical steel bridges, which are 2.5 mm at the horizontal symmetry axis. The permanent magnet material is VACODYM 362/140 and the electrical steel is an arbitrary one with 2.0 T saturation polarization.

In order to magnetize the magnets, the coils are excited with the current illustrated in Figure 3 b. The current was produced in[20] by an impulse magnetizer to magnetize NdFeB magnets in an air-cored coil. The amplitude of the impulse current at 100% is 1200 A and is varied by multiplication factors mag_{mul} to achieve different magnetization sates. The excitation and therefore the transient simulation is divided into 500 equidistant time steps to be sufficiently accurate. It is assumed that the laminated electrical steel of the rotor is nonconductive. The electrical conductivity of the magnet is assumed to 70 000 S/m.

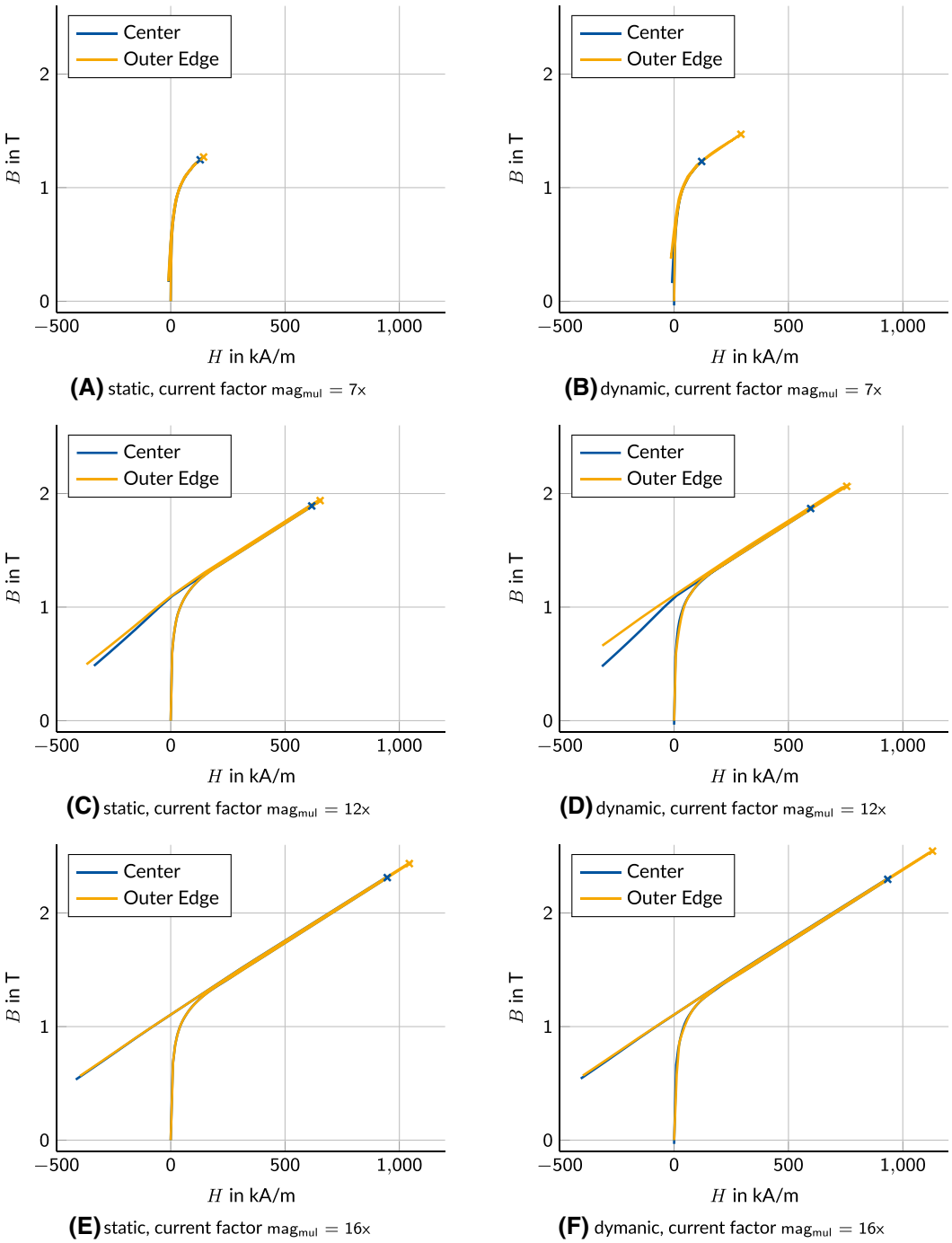

FIGURE 8 Comparison of demagnetization curves with and without eddy currents

In Figure 7A-F, the local flux density distribution of the spoke-type rotor are depicted for different amplitudes of impulse magnetization currents, $I_peak*mag_{mul}$. At the beginning of the transient simulation, the magnetic flux concentrates at the small steel bridges surrounding the magnet, because of their lower magnetic resistance. This is due to the higher magnetic resistance of the magnetizing curve of the magnet as well as induced eddy currents inside the magnet, which counteract the penetrating field. As a result, the magnet begins to magnetize only after the rotor bridges are saturated. Since the eddy currents strongly counteract the penetration of the field, the magnetic flux has to pass the saturated rotor bridges. Because of the smaller cross-section, the right-hand bar first goes into saturation and the magnetic flux density enters from the right side into the magnet. This results in an inhomogeneous field distribution inside the magnet. Some time steps later, also the left bridge is saturated and the magnetic flux density enters from the left side of the magnet. The different change of the magnetic flux penetration at both sides creates eddy currents that are distributed unsymmetrically to the center of the magnet. To sum up the geometry, determining the reluctance network has a strong influence on the flux density and eddy-current distribution. The flux caused by the inner coil encloses a smaller area compared with the outer coil, whereby the flux density of the inner rotor surface is higher than on the outer rotor surface, which spreads back to the magnets due to the curvature of the rotor. For the lowest current amplitude, there is a small remanence on the right side of the magnet, but the magnet is self-degaussing over the two steel bridges. In all simulations, the center of the magnetization is slightly shifted to the right, which is recognizable by the distribution of the equipotential lines of the magnetic vector potential. The distance between the equipotential lines decreases to the edges of the magnet, corresponding to an increasing flux density at the edges. The shift of the center of magnetization from the center of the magnet decreases by increasing the amplitude of impulse magnetization current. A homogeneous magnetization is almost reached at the highest current amplitude. The magnetized magnet locally demagnetizes at the edges over the steel bridges. The impact of eddy currents is visualized in Figure 8, which sets the simulations with and without eddy currents against each other. It can be clearly seen that the eddy currents reduce the magnetic field in the center and increase it at the edges of the permanent magnet. A purely static consideration of the maximum magnetization field can therefore lead to an erroneous assessment of the magnetization requirement. The mentioned rule of thumb, concerning at least three or up to five times of the coercivity for full magnetization, can now be tailored exactly to the material and the geometry.

5 | CONCLUSIONS

The magnetizing field strength-dependent demagnetization behavior of permanent magnets in the first and second quadrants is modeled by the history-dependent model. For this purpose, the maximum experienced field strength is stored in each element. Based on an anisotropic behavior, only a magnetic polarization is considered in the preferred direction and is neglected in the other directions. To handle the nonlinear material behavior, a quasi Newton method for the FEM is introduced. Eddy currents in the material are considered and their influence on the local distribution of magnetization is investigated. In the magnetization process of the spoke-type rotor of a permanent magnet synchronous machine, eddy currents lead to inhomogeneous magnetization as long as the magnetizing field does not reach a necessary saturation threshold. An inhomogeneous magnetization by eddy currents during magnetization is amplified at demagnetization by the different demagnetization characteristics. An extension of the model around return lines and remagnetization is conceivable. Based on this, investigations on the magnetization of rotor magnets by multiple magnetization can be done.[3]

ACKNOWLEDGEMENTS

This work was developed in the context of a German Research Foundation (DFG) grant for project: 373150943-Vector hysteresis modeling of ferromagnetic materials.

ORCID

Gregor Bavendiek https://orcid.org/0000-0002-3731-8800

REFERENCES

1. Chikazumi S. *Physics of magnetism*, *Wiley Series on the Science and Technology of Materials*: Wiley; 1964.
2. Hsieh MF, Hsu YC, Dorrell DG. Design of large-power surface-mounted permanent-magnet motors using postassembly magnetization. *IEEE Trans Ind Electron*. 2010;57(10):3376-3384.

3. Hsieh MF, Lien YM, Dorrell DG. Postassembly magnetization of rare-earth fractional-slot surface permanent-magnet machines using a two-shot method. *IEEE Trans Ind Appl*. 2011;47(6):2478-2486.
4. Bastos JPA, Sadowski N. *Magnetic Materials and 3D Finite Element Modeling*. Boca Raton: CRC Press; 2013.
5. Zhou P, Lin D, Xiao Y, Lambert N, Rahman MA. Temperature-dependent demagnetization model of permanent magnets for finite element analysis. *IEEE Trans Magn*. 2012;48(2):1031-1034.
6. Steentjes S, Petrun M, Glehn G, Dolinar D, Hameyer K. Suitability of the double Langevin function for description of anhysteretic magnetization curves in NO and GO electrical steel grades. *AIP Advances*. 2017;7(5):56013.
7. Harrison RG. Positive-feedback theory of hysteretic recoil loops in hard ferromagnetic materials. *IEEE Trans Magn*. 2011;47(1):175-191.
8. Zhu X, Quan L, Chen D, Cheng M, Hua W, Sun X. Electromagnetic performance analysis of a new stator-permanent-magnet doubly salient flux memory motor using a piecewise-linear hysteresis model. *IEEE Trans Magn*. 2011;47(5):1106-1109.
9. Glehn G, Steentjes S, Hameyer K. Pulsed-field magnetometer measurements and pragmatic hysteresis modeling of rare-earth permanent magnets. *IEEE Trans Magn*. 2018;54(3):1-4.
10. Egorov D, Petrov I, Link J, Stern R, Pyrhönen JJ. Model-based hysteresis loss assessment in PMSMs with ferrite magnets. *IEEE Trans Ind Electron*. 2018;65(1):179-188.
11. Zhang D, Kim H, Li W, Koh C. Analysis of magnetizing process of a new anisotropic bonded NdFeB permanent magnet using FEM combined with Jiles-Atherton hysteresis model. *IEEE Trans Magn*. 2013;49(5):2221-2224.
12. Koh CS, Hong SK. Finite element analysis of magnetizer using Preisach model. *IEEE Trans Magn*. 1999;35(3):1227-1230.
13. Bergqvist A, Lin D, Zhou P. Temperature-dependent vector hysteresis model for permanent magnets. *IEEE Trans Magn*. 2014;50(2):345-348.
14. Vacuumschmelze. Rare-earth permanent magnets.
15. Binns KJ, Lawrenson PJ, Trowbridge CW. *The analytical and numerical solution of electric and magnetic fields*, Chapter 1 (pp. 1-20). Reprint. with corr. in paperback September 1995. Chichester [u.a.]: Wiley; 1995.
16. Gilat A. *Numerical Methods : An Introduction with Applications Using MATLAB*, 2nd ed. Hoboken, NJ: Wiley; 2011.
17. Leite JV, Benabou A, da Silva PA, et al. Analysis of a rotational single sheet tester using 3D finite element model taking into account hysteresis effect. *COMPEL - The International Journal for Computation and Mathematics in Electrical and Electronic Engineering*. 2007;26(4):1037-1048. https://www.emerald.com/insight/content/doi/10.1108/03321640710756366/full/html
18. Neagoe C, Ossart F. Analysis of convergence in nonlinear magnetostatic finite elements problems. *IEEE Trans Magn*. 1994;30(5):2865-2868.
19. Silvester PP, Ferrari RL. *Finite Elements for Electrical Engineers*, Third edition. Cambridge: Cambridge University Press; 1996.
20. Przybylski M, Kapelski D, Ślusarek B, Wiak S. Impulse magnetization of Nd-Fe-B sintered magnets for sensors. *Sensors*. 2016;16(4).
21. Bavendiek G, Hameyer K, Filippini M, Alotto P. Analysis of impulse-magnetization in rare-earth permanent magnets. *Int J Appl Electromagn Mech*. 2018;57(S1):23-31.
22. Seol H, Jeong T, Jun H, Lee J, Kang D, IEEE Trans Magn. Design of 3-times magnetizer and rotor of spoke-type PMSM considering postassembly magnetization. 2017;53(11):1-5.
23. Kim K, Park M, Kim H, Chai S, Hong J. Estimation of rotor type using ferrite magnet considering the magnetization process. *IEEE Trans Magn*. 2016;52(3):1-4.

How to cite this article: Bavendiek G, Müller F, Steentjes S, Hameyer K. Modeling of history-dependent magnetization in the finite element method on the example of a postassembly rotor magnetizer. *Int J Numer Model*. 2019;e2674. https://doi.org/10.1002/jnm.2674